Journal of Wind Engineering & Industrial Aerodynamics 197 (2020) 104081

Contents lists available at ScienceDirect

Journal of Wind Engineering & Industrial Aerodynamics

journal homepage: www.elsevier.com/locate/jweia

Numerical study on suppression of vortex-induced vibration of circular cylinder by helical wires

Takeshi Ishihara, Tian Li *

Department of Civil Engineering, School of Engineering, The University of Tokyo, Tokyo, 113-8656, Japan

ARTICLE INFO

Keywords:
Suppression of VIV
Circular cylinder
Helical wire
LES turbulence model

ABSTRACT

The mechanism of suppression for the vortex-induced vibration (VIV) of circular cylinder by the helical wires is investigated using LES turbulence model. Numerical models for the free-vibrating circular cylinders with and without the helical wires are proposed and validated by the experiments. Simulations are carried out for a large mass ratio of 248 and a small damping ratio of 0.00257 with the Reynolds numbers ranging from 16000 to 24500 and the reduced velocities ranging from 4.5 to 6.8. It is noticed that the helical wires of diameters ratio $d/D = 0.1$ effectively suppress the amplitude of VIV by nearly 80% and avoid the "lock in". The steady and unsteady aerodynamic forces of circular cylinders with and without the helical wires as well as the flow patterns are also examined to clarify the mechanism of VIV suppression. It is found that the fluctuating lift forces and their spanwise correlation for the wired cylinder are significantly reduced comparing with those for the bare cylinder, due to the enhancement of three-dimensional disturbance to the wake caused by helical wires. The aerodynamic damping for the oscillated bare cylinder is negative, while that for the wired cylinder is positive with a vibration amplitude $A/D = 0.1$ at the resonance velocity of bare cylinder.

1. Introduction

When a circular cylinder is immersed into a steady flow, vortices are shed from alternating sides of the cylinder. The latter is then subjected to the unsteady drag and lift forces. These forces may induce vibration of the cylinder, namely vortex-induced vibration, which affects the shedding of the vortices in turn. This interaction between the flow and the cylinder forms a highly nonlinear and complex phenomenon. It will not only increase the dynamic load on the structures but also influence the structural stability. The vibrations may accelerate the fatigue failure and increase the expenses for maintenance and replacement.

During the last decades, the VIV has been extensively investigated through the canonical problem of a rigid circular cylinder elastically mounted in the cross-flow direction by experiments. Feng (1968) firstly conducted an experiment of an elastically mounted cylinder in air at high mass ratios defined as $m^* = 4m/(\pi\rho D^2 L)$ and demonstrated that the resonance of the cylinder occurs over a regime of reduced velocity U_r defined by $U_r = U/f_n D$, where m, L and D are the mass, length and diameter of the cylinder respectively. ρ *is* the fluid density, U is the free-stream velocity and f_n is the natural frequency of structure. More studies focused on the VIV in water, where the mass ratios are generally 1 to 3 orders of magnitude smaller than those in air. The VIV in water happens for a wider regime of reduced velocity and the branches of response are different compared with the phenomena in air (Khalak and Williamson, 1997). Comprehensive reviews of various aspects of VIV can be found in the publications of Sarpkaya (2004), Williamson and Govardhan (2008) and Bearman (2011). The research for VIV of other shapes of cylinder can be found in Zhao et al. (2013) and Singh and Biswas (2013).

A wide variety of aerodynamic and hydrodynamic countermeasures for suppressing vortex shedding was used and divided into three categories (Zdravkovich, 1981): (1) surface protrusions (helical strakes, wires, fins, studs or spheres, etc.), which affect separation lines and/or separated shear layers; (2) shrouds (perforated, gauze, axial-rods, axial slats, etc.), which affect the entrainment layers; (3) nearwake stabilisers (splitter plates, guiding vanes, base-bleed, slits cut across the cylinder, etc.), which prevent interaction of entrainment layers. More recently, suppression of vortex shedding by thermal effects was mentioned by Kakade et al. (2010), Arif and Hasan (2019) and Zafar and Alam (2019). Among these devices, helical strakes have been proven effective and widely used in various industrial and offshore applications to suppress fluid-induced vibration.

* Corresponding author.
E-mail address: li@bridge.t.u-tokyo.ac.jp (T. Li).

https://doi.org/10.1016/j.jweia.2019.104081
Received 25 September 2019; Received in revised form 25 December 2019; Accepted 25 December 2019
Available online xxxx
0167-6105/

Scruton and Walshe (1963) firstly invented efficient helical strake of sharp-edged rectangular section to avoid wind-excited oscillations of cylindrical structures. It is effective to suppress VIV at a wide range of Reynolds number (Allen et al., 2006), and narrows or even avoids the "lock in" region of amplitude response (Bearman and Brankovic, 2004; Zhou et al., 2011; Quen et al., 2014). As an alternative equipment, helical wires of rounded section are considered to be of great practical significance because of the ease of installation on cylindrical structures and the insensitivity of flow direction same as helical strakes. In addition, the drag coefficient of cylinder with helical strakes is increased by their sharp edge (Korkischko et al., 2007), which is possible to be avoid by using wires of rounded section (Hover et al., 2001). However, current design practices of helical wires rely heavily on the model testing, because the vibration control mechanism of such fluid dynamic countermeasures has not been fully understood and it is still hard to make a guidance to select a suitable configuration for cylinder structures experiencing similar problems. More comprehensive study on this issue and related design criteria is necessary to concern their effectiveness and mechanism.

To investigate the mechanism of suppression countermeasures for flow-induced vibration, the numerical simulation of fluid-structure interaction (FSI) is considered as a powerful tool. It provides a simultaneous vision of the wake patterns, fluid forces and dynamic responses, which allows a coupled analysis of the fluid-structure system. However, some aspects of current deficiency for the simulation of VIV can be summarized from previous studies as below: (1) The greater part of previous studies on the VIV of a circular cylinder were conducted using two-dimensional simulation (Guilmineau and Queutey, 2002; Leontini et al., 2006; Pan et al., 2007; Tu et al., 2014; Wanderley and Soares, 2015; Kang et al., 2017). As the simulations of fluid-structure interaction of vibrating cylinders need smaller time step and longer calculation time than those for the stationary cylinders, massive computational resources are required for the three-dimensional simulation. However, the flow in the wake of a circular cylinder is three-dimensional when the Reynolds number exceeds 200 (Williamson, 1988). Also, the three-dimensional model is necessary for the simulation of helical structures. (2) Most of numerical studies on the VIV over the past few decades focused on the low Reynolds number flows of $Re = 100–5000$ (Lucor et al., 2005; Singh and Mittal, 2005; Navrose and Mittal, 2013; Zhao et al., 2014; Gsell et al., 2016; Wang et al., 2017), in which fundamental fluid dynamics of phenomena were explored, while the Reynolds number regime of turbulent boundary layer is necessary to study where most of structures are located in and the related VIV is the most considerable. The Reynolds number is known to have a significant impact on the VIV behaviour as well (Govardhan and Williamson, 2006; Raghavan and Bernitsas, 2011). (3) Although numerical methods have been widely used to study the mechanism of VIV for the bare cylinder, only a few of researchers considered cylinders with the helical strake since the three-dimensional numerical model and the technique to deal with their complex geometry are necessary (Constantinides and Oakley, 2006; Pinto et al., 2006; Pontaza et al., 2009; Carmo et al., 2012). The disturbance of flow field as well as the vibration suppression effect by the helical strake were found in their studies, but further work is still needed to explain the mechanism of these phenomena. Moreover, there is no numerical study on helical wires and their effects have not been clarified yet. (4) Most of the previous numerical studies of VIV mentioned above used the fluid media of water, which results in very low mass ratios. Few investigations were performed with the high mass ratios (Bahmani and Akbari, 2010), which is often encountered in wind engineering.

In this study, VIV suppression by helical wires for circular cylinders in air is investigated using LES turbulence model. The numerical model, mesh and modelling of oscillation system for cylinders with and without helical wires are shown in Section 2. The numerical model is validated by the experiments and the effects of helical wires on the aerodynamic forces and VIV of circular cylinder are studied in Section 3. The suppression mechanism of helical wires for the VIV of circular cylinder is also clarified by analysing the steady and unsteady forces on the cylinders in this Section. The conclusions are summarized in Section 4.

2. Numerical model

The numerical model used in this study is explained in this section. The governing equations and solution schemes are given in Section 2.1. The computational domain and mesh are described in Section 2.2 and the modelling of oscillation system is introduced in Section 2.3.

2.1. Governing equations and schemes

The governing equations for the flow are the unsteady incompressible Navier-Stokes equations with LES turbulence model, which are derived by filtering continuity and Navier-Stokes equations in a moving mesh system as

$$\frac{\partial \rho \tilde{u}_i}{\partial x_i} = 0 \tag{1}$$

$$\frac{\partial}{\partial t}(\rho \tilde{u}_i) + \frac{\partial \rho \tilde{u}_i}{\partial x_j}(\tilde{u}_j - \widehat{u}_j) = \frac{\partial}{\partial x_j}\left(\mu \frac{\partial \tilde{u}_i}{\partial x_j}\right) - \frac{\partial \tilde{p}}{\partial x_i} - \frac{\partial \tau_{ij}}{\partial x_j} \tag{2}$$

where x is the coordinate, u is the velocity, p is the pressure and t is the time. The subscript i and j stand for different directions in Cartesian coordinates, which include the streamwise, spanwise and vertical directions. The "~" denotes the filtered component and $\widehat{u}$ is the velocity component of the moving mesh. μ is the viscosity of fluid and τ_{ij} is the subgrid-scale stress defined by

$$\tau_{ij} = \rho \tilde{u}_i \tilde{u}_j - \rho \widetilde{u_i u_j} \tag{3}$$

The subgrid-scale stresses resulting from the filtering operations are unknown, and they are modelled as

$$\tau_{ij} = -2\mu_t \tilde{S}_{ij} + \frac{1}{3}\tau_{kk}\delta_{ij} \tag{4}$$

where μ_t is the subgrid-scale turbulent viscosity, and δ_{ij} is the Kronecker delta. $\tilde{S}_{ij}$ is the rate-of-strain tensor for the resolved scale defined as

$$\tilde{S}_{ij} = \frac{1}{2}\left(\frac{\partial \tilde{u}_i}{\partial x_j} + \frac{\partial \tilde{u}_j}{\partial x_i}\right) \tag{5}$$

The wall-adapting local-eddy viscosity model (WALE) (Nicoud and Ducros, 1999) is used to model the subgrid-scale turbulent viscosity μ_t as

$$\mu_t = \rho L_s^2 \frac{\left(S_{ij}^d S_{ij}^d\right)^{3/2}}{\left(\tilde{S}_{ij}\tilde{S}_{ij}\right)^{5/2} + \left(S_{ij}^d S_{ij}^d\right)^{5/4}} \tag{6}$$

where the mixing length L_s of subgrid-scales and S_{ij}^d in the WALE model are defined as

$$L_s = \min\left(\kappa\delta, C_w V^{1/3}\right) \tag{7}$$

$$S_{ij}^d = \frac{1}{2}\left(\overline{g}_{ij}^2 + \overline{g}_{ji}^2\right) - \frac{1}{3}\delta_{ij}\overline{g}_{kk}^2, \quad \overline{g}_{ij} = \frac{\partial \tilde{u}_i}{\partial x_j} \tag{8}$$

where κ is the von Karman constant and is taken equal to 0.42. C_w is a constant in the WALE model set as 0.325. δ is the distance to the closest wall, and V is the volume of a computational cell.

The advantage of the WALE model is that it returns a zero turbulent viscosity for the laminar shear flows. This allows the correct treatment of laminar zones for the Reynolds number of subcritical domain in this paper. In contrast, the Smagorinsky-Lilly model (Smagorinsky, 1963) produces nonzero turbulent viscosity.

For the wall-adjacent cells, when they are in the laminar sub-layer, the wall shear stress is obtained from the laminar stress-strain relationship as

$$\frac{\tilde{u}}{u_\tau}=\frac{\rho u_\tau y}{\mu} \tag{9}$$

where $\tilde{u}$ is the filtered velocity that is tangential to the wall; u_τ is the friction velocity; y is the distance between the center of the cell and the wall. If the mesh cannot resolve the laminar sub-layer, it is assumed that the centroid of the wall-adjacent cells falls within the logarithmic region of the boundary layer, and the law-of-the-wall is employed as

$$\frac{\tilde{u}}{u_\tau}=\frac{1}{\kappa}\ln E\left(\frac{\rho u_\tau y}{\mu}\right) \tag{10}$$

where the constant E is taken equal to 9.8.

The filtered Navier-Stokes equations are solved with the commercial CFD code ANSYS Fluent 16.2 (ANSYS Inc, 2015) using the control volume method. The second-order central difference scheme is used for the convective and viscosity terms, and the second-order implicit scheme is used for the unsteady term. SIMPLE (Semi-Implicit Method for Pressure Linked Equations) algorithm is employed for solving the discretized equations (Ferziger and Peric, 2002). The simulations were performed on the parallel computing cluster system in the Bridge and Structure Laboratory of the University of Tokyo (Intel Xeon CPU E5-2630 v2, 240 cores, 128 GB memory). The simulation with 80 cores takes about 150 h for each reduced velocity.

2.2. Computational domain and mesh

The circular cylinders with and without helical wires are simulated in this study. The computational domain is shown in Fig. 1, whose width and depth are 50D and 30D respectively. The spanwise length of the domain in this paper was 4D, referred to the previous CFD study of circular cylinder (Prsic et al., 2014) that this length is enough to simulate the correlation length of circular cylinder in the spanwise direction. The helical wire is chosen as 4-start configuration with pitch $P = 8D$ and diameter $d = 0.1D$, which is effective for the VIV suppression reported by Weaver (1959). Thus each helical wire rotates 180° along the spanwise direction with the spanwise length $L = 4D$, provides a central symmetric and periodic pattern which is effective to predict aerodynamic forces for long cylinders using the symmetric boundary condition at the end of cylinder in simulation. The cylinder is located 15D downstream from the inlet. For the unsteady analysis where the cylinder is subjected to oscillations, the sliding mesh technique is employed at an interface located 10D downstream from the inlet to allow oscillations. The left side of interface is fixed while the right side can move transversely, combining with dynamic laying mesh technique used in the transverse boundary. Uniform velocity condition is specified at the inlet boundary, and zero diffusive condition is used at the outlet boundary. Symmetric condition is used for top, bottom and transverse surfaces of the domain.

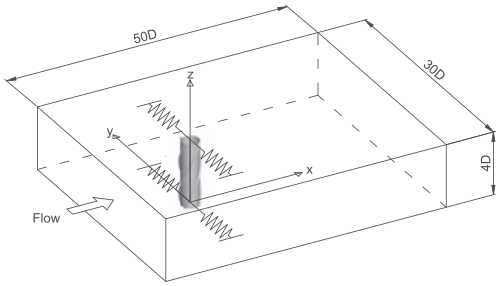

Fig. 1. Overview of computational domain.

An enlarged view of the mesh in the vicinity of helical wires is shown in Fig. 2. Since the helical wire is much smaller in size compared to the cylinder section, it requires a high resolution to capture the flow accurately. The wedge mesh is employed around the wire connected with hexahedron mesh around the other parts of circular cylinder to ensure the accuracy in the region close to the complex geometry of helical wires. A hybrid mesh system is used and divided into several zones. The inner mesh is formed by sweeping the two-dimensional mesh in the spanwise direction and twisting the mesh at the same time, which builds the helical pattern for the wires. The outer mesh is swept along the spanwise direction rigidly. The twisted inner mesh around cylinder is connect with the outer mesh using a non-matching interface as shown as a red circle. The mesh sizes of both sides of the interface are similar, thus the accuracy can be kept. This mesh system not only helps to generate a reasonable mesh, but also allows a use of less quantity of mesh to speed up the calculation with a sufficient accuracy.

The convergence of mesh is tested through several non-dimensional aerodynamic coefficients of the bare and wired cylinders, namely the drag and lift coefficients as well as the Strouhal number. The drag and lift coefficients are defined as $C_D = F_D/(0.5\rho U^2 DL)$ and $C_L = F_L/(0.5\rho U^2 DL)$, where F_D and F_L are the drag and lift forces obtained by integrating pressure and friction over the cylinder surface. The cylinder diameter D used to calculate aerodynamic coefficients is kept as the value for the bare cylinder even when helical wires are attached. The Strouhal number is expressed by $St = f_v D/U$, where f_v represents the frequency of vortex shedding obtained by the spectrum analysis of lift force on cylinders. The mean drag coefficient $C_{D\ mean}$, the root mean square of lift coefficient $C_{L\ rms}$ and the Strouhal number St predicted by meshes with different resolutions are shown in Table 1. The mesh resolution is increased gradually from Mesh 1 to Mesh 3 for the bare and wired cylinders respectively. The change ratios are shown in brackets. It is noticed that the difference of results between Mesh 2 and Mesh 3 is less than 3% for both bare and wired cylinders, which is acceptable for engineering applications for convergence. Thus, Mesh 2 is used in the following simulations in consideration of both accuracy and efficiency.

2.3. Modelling of oscillation system

VIV is the excitation caused by the fluid forces and the modelling of fluid-structure interaction is required. Since the vortex-induced vibration mainly occurs in the transverse direction, this system can be simplified as

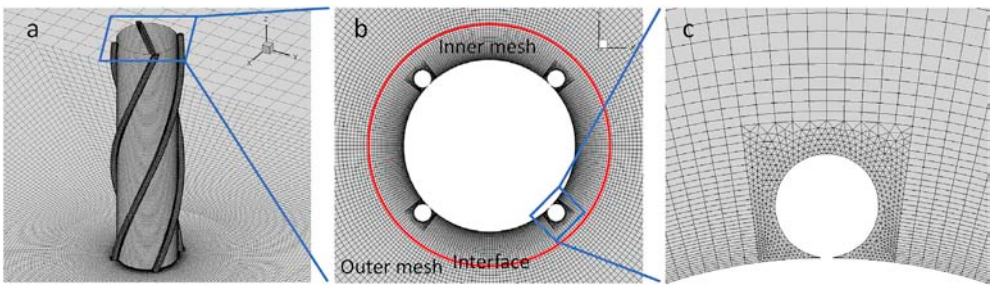

Fig. 2. Mesh near the wired cylinder: (a) bird view; (b) top view; (c) view of the mesh near wires.

Table 1
Mesh convergence test.

	Mesh quantity	$C_{D\ mean}$	$C_{L\ rms}$	St
Bare cylinder-Mesh 1	3,251,400	1.3046	0.5407	0.1857
Bare cylinder-Mesh 2	5,931,000	1.2504 (4.2%)	0.5128 (5.2%)	0.1946 (4.8%)
Bare cylinder-Mesh 3	8,012,640	1.2354 (1.2%)	0.5026 (2.0%)	0.1955 (0.5%)
Wired cylinder-Mesh 1	3,531,000	1.3345	0.0713	0.1583
Wired cylinder-Mesh 2	5,932,320	1.2715 (4.7%)	0.0677 (5.0%)	0.1610 (1.7%)
Wired cylinder-Mesh 3	8,674,320	1.2533 (1.4%)	0.0659 (2.7%)	0.1623 (0.8%)

a single degree of freedom (SDOF) system, where the structural flexibility can be modelled by using a mass-spring system in the transverse direction as

$$m\ddot{y} + c\dot{y} + ky = F_y(t) \tag{11}$$

where m is the structural mass, c is the structural damping, k is the structural stiffness and $F_y(t)$ is the time dependent transverse force acting on the model. In this study, these structural parameters are set the same as the experiment (Feng, 1968) to keep two important parameters consistent with those in the experiment, namely, mass ratio $m^* = 248$ and damping ratio $\zeta = c/(2m\omega_n) = 0.00257$, where ω_n is the natural angular frequency of the cylinder, resulting a combined mass-damping parameter $m^*\zeta = 0.64$ and Scruton number $Sc = \pi^2 m^* \zeta = 6.28$. The amplitude of VIV decreases with the combined mass-damping parameter $m^*\zeta$, as shown in the Griffin plot (Griffin, 1980). The detailed information about the influence of m^*, ζ and their combined parameter $m^*\zeta$ on the characteristics of VIV can be found in Khalak and Williamson (1997) and Bahmani and Akbari (2010). The time dependent force $F_y(t)$ in the right hand side of Eq. (11) is obtained by integrating the fluid pressure and friction force on the cylinder surface. To analyze the structural response of this SDOF system, the equation of motion is solved using the fourth-order Runge-Kutta method (Sarwar and Ishihara, 2010). The sliding mesh is used to update the dynamic domain during the simulation because of the higher accuracy for the large-amplitude motion compared with other dynamic mesh methods such as the remeshing (Ferziger and Peric, 2002).

3. Results and discussion

The numerical results are discussed in this section. The numerical model is firstly validated by experiments in Section 3.1. The free vibration of bare and wired cylinders are then investigated in Section 3.2. Finally, the mechanism of VIV suppression is explained by the steady and unsteady aerodynamic forces for the bare and wired cylinders in Sections 3.3 and 3.4 respectively.

3.1. Validation of numerical models

The aerodynamic forces on cylinder should be simulated accurately for the prediction of VIV. Two key factors significantly influence the accuracy of simulation. One is the length of cylinder and the other is the boundary condition at the end of cylinder.

For the length of cylinder, the distribution of mean pressure coefficient on the surface of bare cylinder is used to check its influence. The pressure coefficient is defined as $C_p=(p-p_{ref})/(0.5\rho U^2)$ where p_{ref} is the referred pressure in the undisturbed flow. The distribution of mean pressure coefficient $C_{p\ mean}$ on the cylinder surface is compared with the experimental data (West and Apelt, 1982; Lim and Lee, 2002; Kubo et al., 2012) with the cylinder length $L = 1D$ and $4D$ as shown in Fig. 3, where θ

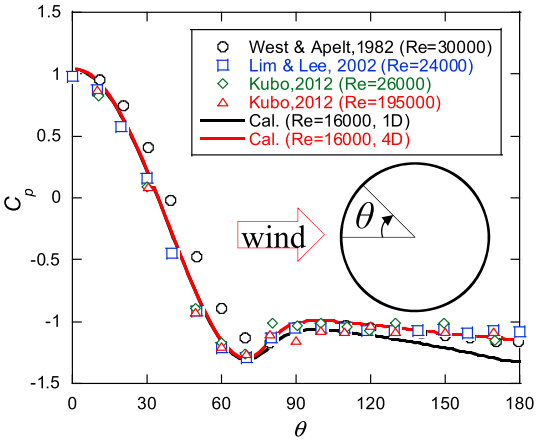

Fig. 3. Mean pressure coefficient on the bare cylinder.

$= 0°$ corresponds to the flow-stagnation point in the frontal surface. The experiment by Kubo et al. (2012) shows that the pressure distributions are consistent if the Reynolds number are in the subcritical regime. In this study, the simulations for the free vibrating cylinder is under $Re = 16000–24500$, the fixed and forced vibrating bare cylinders are under $Re = 16000$, and the fixed and forced vibrating wired cylinders are under $Re = 70000$ and 16000, which always belong to the subcritical regime, thus the Reynolds number effect can be neglected for the steady pressure distribution. It is noticed that the windward pressure is predicted well with both numerical models of $L = 1D$ and $4D$. The leeward pressure predicted by the numerical model of $L = 4D$ shows good agreement with the experimental data, while the value by the $1D$ model is underestimated. It implies that the model length $L = 4D$ is necessary. Fig. 4 shows the pattern of mean streamlines around the bare cylinder for the case of $L = 4D$, in which the angle of separation is around θ=90° and 270°, agrees with the previous study in the subcritical regime (Prsic et al., 2014).

For the boundary condition at the end of cylinder, periodic and symmetric boundaries are the possible choices. In this study, the correlation coefficient of lift force with these two boundaries are compared for the bare cylinder. Five cross-sections (CS) are monitored to calculate the correlation coefficient as shown in Fig. 5, where CS1 is set as the base section. The correlation coefficient γ_{1a} between CS1 and CSa (cross section a) is calculated as

$$\gamma_{1a} = \frac{\sum_{t_x}^{t_y}(C_{L1} - \overline{C_{L1}})\ (C_{La} - \overline{C_{La}})}{\left(\left(\sum_{t_x}^{t_y}(C_{L1} - \overline{C_{L1}})^2\right)\left(\sum_{t_x}^{t_y}(C_{La} - \overline{C_{La}})^2\right)\right)^{0.5}} \tag{12}$$

where C_{La} is the transient lift force coefficient of cross section a. It is shown in Fig. 6 that the correlation coefficients predicted with the

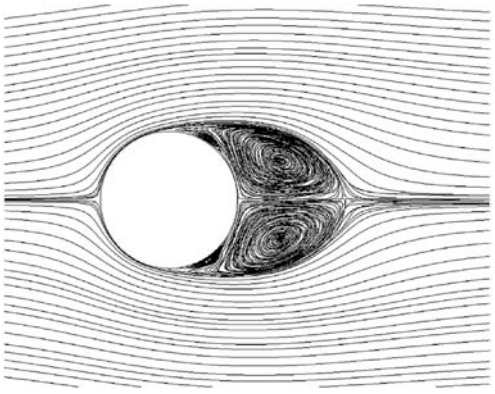

Fig. 4. Mean streamlines around the bare cylinder for the case of $L = 4D$.

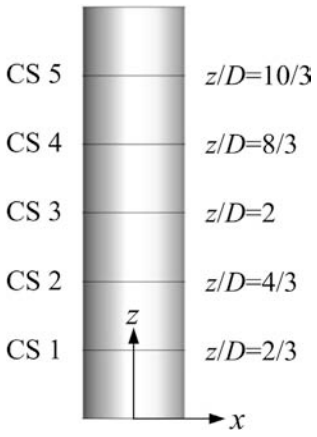

Fig. 5. Tested cross sections of bare cylinder.

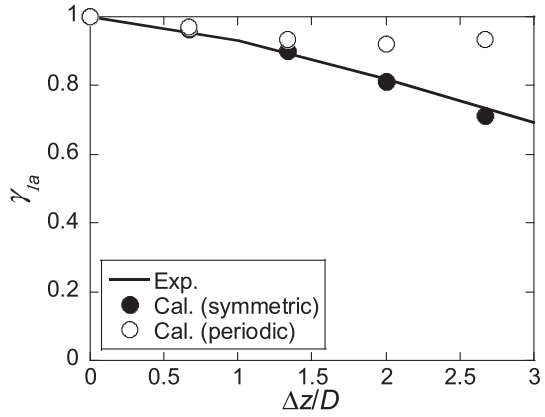

Fig. 6. Correlation coefficient of lift force in the spanwise direction of bare cylinder.

symmetric boundary decrease faster along the spanwise of cylinder than those with the periodic boundary, and are closer to the experimental data by Blackburn (1994).

Furthermore, the mean drag coefficient $C_{D\ mean}$, the root mean square of lift coefficient $C_{L\ rms}$ and the Strouhal number St for the case with the model length of $L = 4D$ and the symmetric boundary condition are compared with those by the previous studies for the bare cylinder (West and Apelt, 1982, 1993; Norberg, 2003) and the wired cylinder (Weaver, 1959) as shown in Table 2. It can be seen that the predicted coefficients agree well with the experimental data.

3.2. Effect of helical wires on vortex-induced vibration of circular cylinder

The free-vibration of the circular cylinders under the reduced velocity U_r from 4.5 to 6.8 is simulated by increasing U_r with a step of 0.58. A smaller step of 0.29 is used near the resonance velocity ($U_r = 5.7$ for the bare cylinder and $U_r = 6.2$ for the wired cylinder) to catch the characteristics of VIV more clearly. Both f_n and D are fixed while U is varied to change U_r in this series of simulations, resulting $Re = 16000–24500$. The oscillation under each U_r is simulated for over 50 periods to get reasonable statistics, and the amplitudes of vibration are determined by averaging the peaks of every period after the vibration gets steady state.

Table 2
Comparison of non-dimensional aerodynamic coefficients of cylinders with previous studies.

Case	$C_{D\ mean}$	$C_{L\ rms}$	St
Bare cylinder			
Present ($Re = 16000$)	1.2504	0.5128	0.1946
West and Apelt (1982, 1993) ($Re = 16000$)	1.2627	0.4673	0.1975
Norberg (2003) ($Re = 16000$)	–	0.46	0.1959
Wired cylinder			
Present ($Re = 70000$)	1.2549	0.0542	0.1603
Weaver (1959) ($Re = 70000$)	–	0.0550	–

The predicted vibration amplitude and vortex shedding frequency are shown in Figs. 7 and 8 compared with the measured results by Feng (1968). The simulation conditions are the same with the experiment. The numerical simulated data is denoted as plot and the experimental one as line, because the vibration characteristics are easily measured with a small step of reduced velocity U_r in the experiments, while numerical simulation is limited in that it takes much longer time to obtain a data point compared with the experiment. It is noticed that the vibration amplitude of bare cylinder firstly increases with the reduced velocity U_r and gets its peak at U_r=5.7, then the amplitude decreases gradually, which shows a typical phenomenon of VIV. The increasing and decreasing branches of response are named as the initial and lower branches following the terminologies of Khalak and Williamson (1999), which exist for the large mass-damping parameter like the current condition. On the other hand, the wired cylinder exhibits a small vibration at U_r=6.2, which is 22% of the peak amplitude for the bare one. The frequency of vortex shedding f_v for the bare cylinder, identified by the lift force spectrum, follows the constant St number of about 0.2 in the unsympathetic region (U_r<5 and >6), while keeps close to the structural natural frequency f_n in the sympathetic region (U_r=5–6), which is an apparent "lock in" regime. The St number for the wired cylinder is

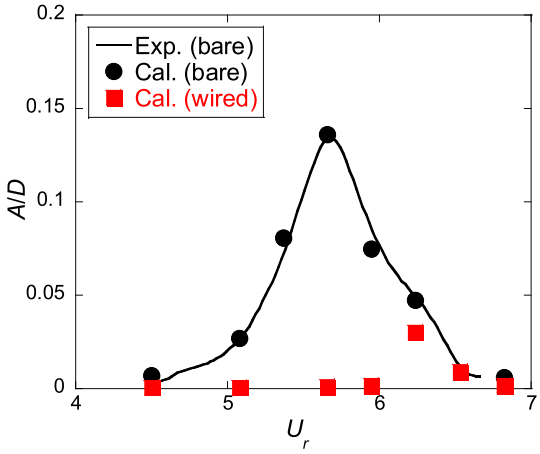

Fig. 7. Variation of amplitude of free vibration with U_r.

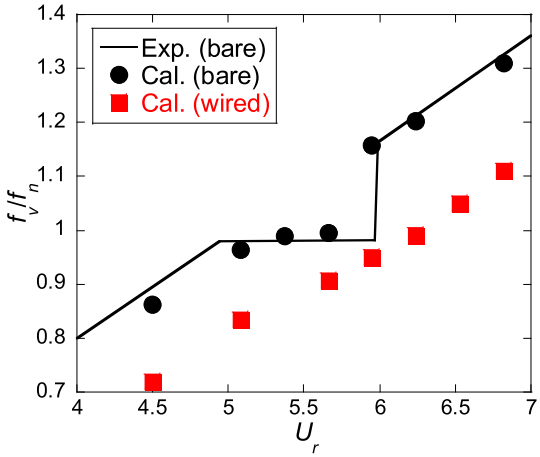

Fig. 8. Ratios of vortex shedding frequency and structural natural frequency.

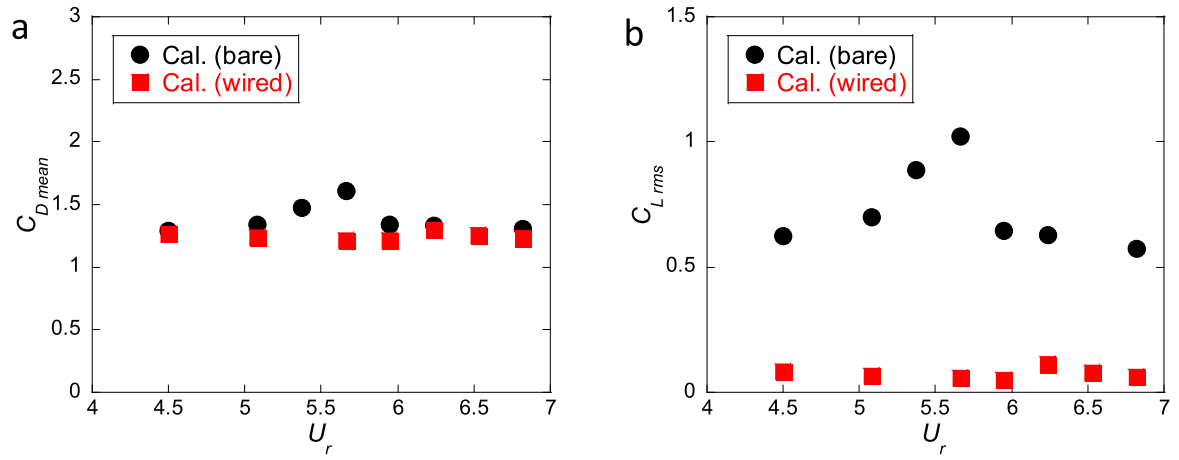

Fig. 9. Aerodynamic force coefficients for the bare and wired cylinders: (a) drag coefficients; (b) lift coefficients.

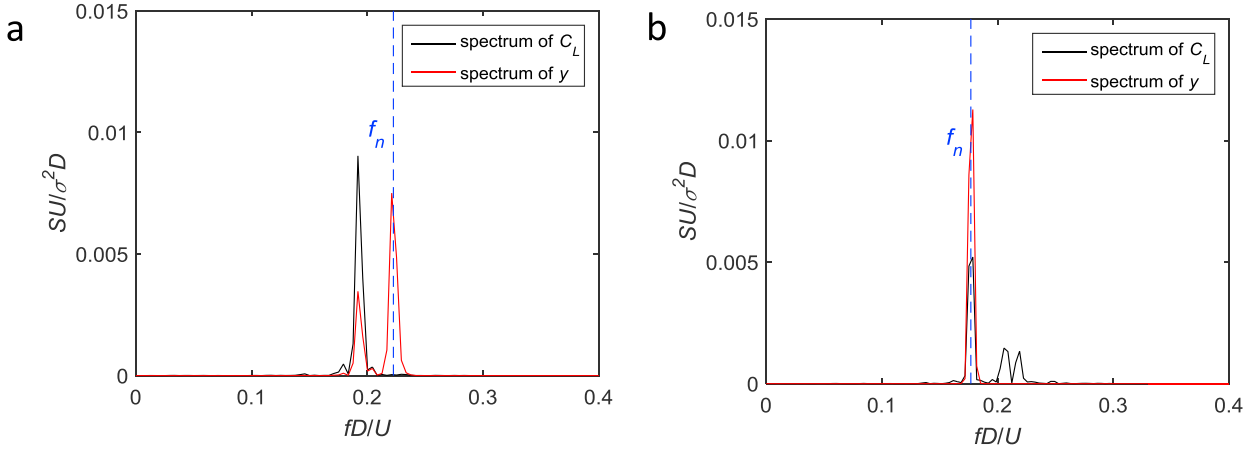

Fig. 10. Spectra of lift coefficient and displacement for the bare cylinder: (a) at the non-resonant regime (U_r=4.5); (b) at the resonant regime (U_r=5.7).

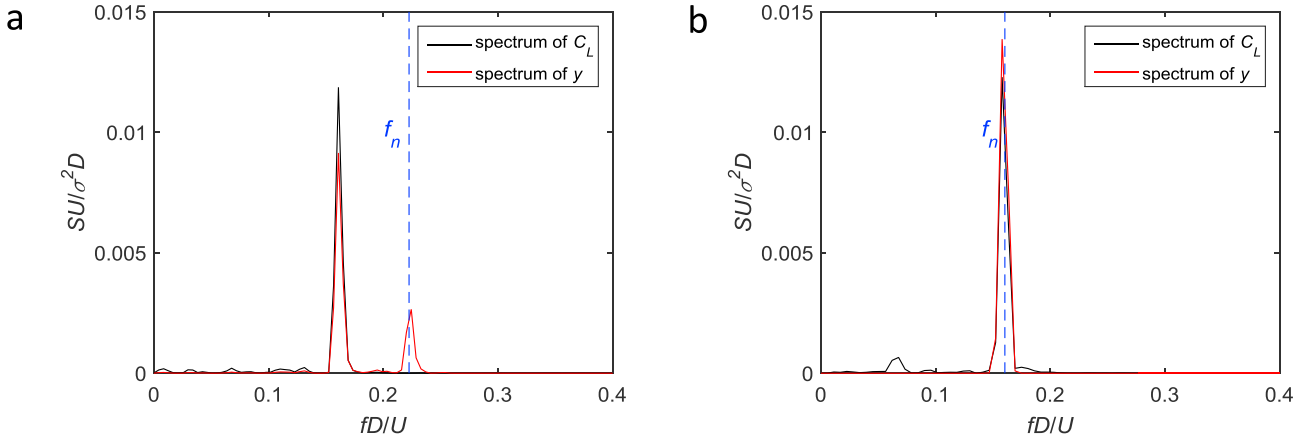

Fig. 11. Spectra of lift coefficient and displacement for the wired cylinder: (a) at the non-resonant regime (U_r=4.5); (b) at the resonant regime (U_r=6.2).

0.16–0.17, which is lower than the value of 0.2 for the bare cylinder since the equivalent diameter of the wired cylinder increases. The vortex shedding frequency of the wired cylinder at U_r=6.2 is close to the structural natural frequency f_n, thus the resonance happens, but "lock in" does not happen for the adjacent U_r.

Fig. 9 illustrates the aerodynamic force coefficients for the bare and wired cylinders. For the bare cylinder, $C_{D\,mean}$ and $C_{L\,rms}$ keep constant for the "non-lock-in" region, but suddenly increase at the sympathetic region caused by the vibration-induced aerodynamic force. These two aerodynamic force coefficients for the wired cylinder keep almost constant over the range of reduced velocity. $C_{D\,mean}$ is not enlarged by the helical wires and $C_{L\,rms}$ are reduced significantly, which is one reason for the vibration suppression and will be discussed in Section 3.3 in detail.

Figs. 10 and 11 show the spectra of lift force coefficient C_L and displacement y obtained from numerical simulations at the non-resonant and resonant regimes for the bare and wired cylinders respectively. The normalized spectrum SU/σ^2D and the normalized frequency fD/U are used to make the spectrum peaks of C_L and y be the similar height, where

f is the frequency, S is the spectrum of C_L or y and σ is the corresponding standard deviation. The spectrum peaks of C_L point out the frequency of vortex shedding f_v and the spectrum peaks of y indicate the oscillating frequency of cylinders. The natural frequency of system f_n is also shown in the figures for comparison. The spectra at the reduced velocity $U_r = 4.5$ and 5.7 are selected for the bare cylinder to show the response in the non-resonant and the resonant regimes. Correspondingly $U_r = 4.5$ and 6.2 are used for the wired cylinder. In the non-resonant regimes as shown in Figs. 10(a) and 11(a), there are two dominating frequencies for displacement y. One is the frequency of vortex shedding f_v and the other is the natural frequency f_n. The phenomena of beats are captured in the time history of displacement y at this regime. However, at the resonant regime as shown in Figs. 10(b) and 11(b), only one dominating frequency exists, namely the frequency of vortex shedding f_v equals to the natural frequency of system f_n.

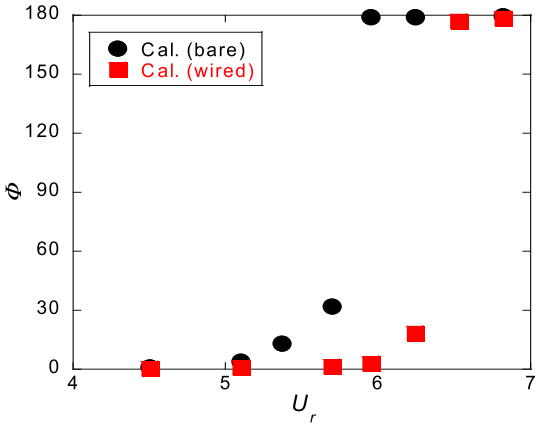

Fig. 12. Phase angle between lift force and displacement.

As mentioned by Khalak and Williamson (1999), there is a phase lag between the displacement and the lift force. Energy will be transferred from the fluid to the structure and excite vibrations if the phase lag equals neither 0° nor 180°. The phase lag Φ is defined as the lead of the lift force over the displacement and calculated using Hilbert transform as shown in Fig. 12. The phase lag Φ is near 0° in initial branch and jumps to about 180° in the lower branch for the bare cylinder, involving an intermittent switching at the resonant regime. This phase jump is similar to those experiments by Khalak and Williamson (1999) and Assi et al. (2010) for the low mass ratio, where the phase lag Φ is near 0° in the initial and upper branches, and jump to 180° in the lower branch. Although the phase lag for the bare cylinder has been studied in the previous researches, it has not been investigated for the wired cylinder. It is found

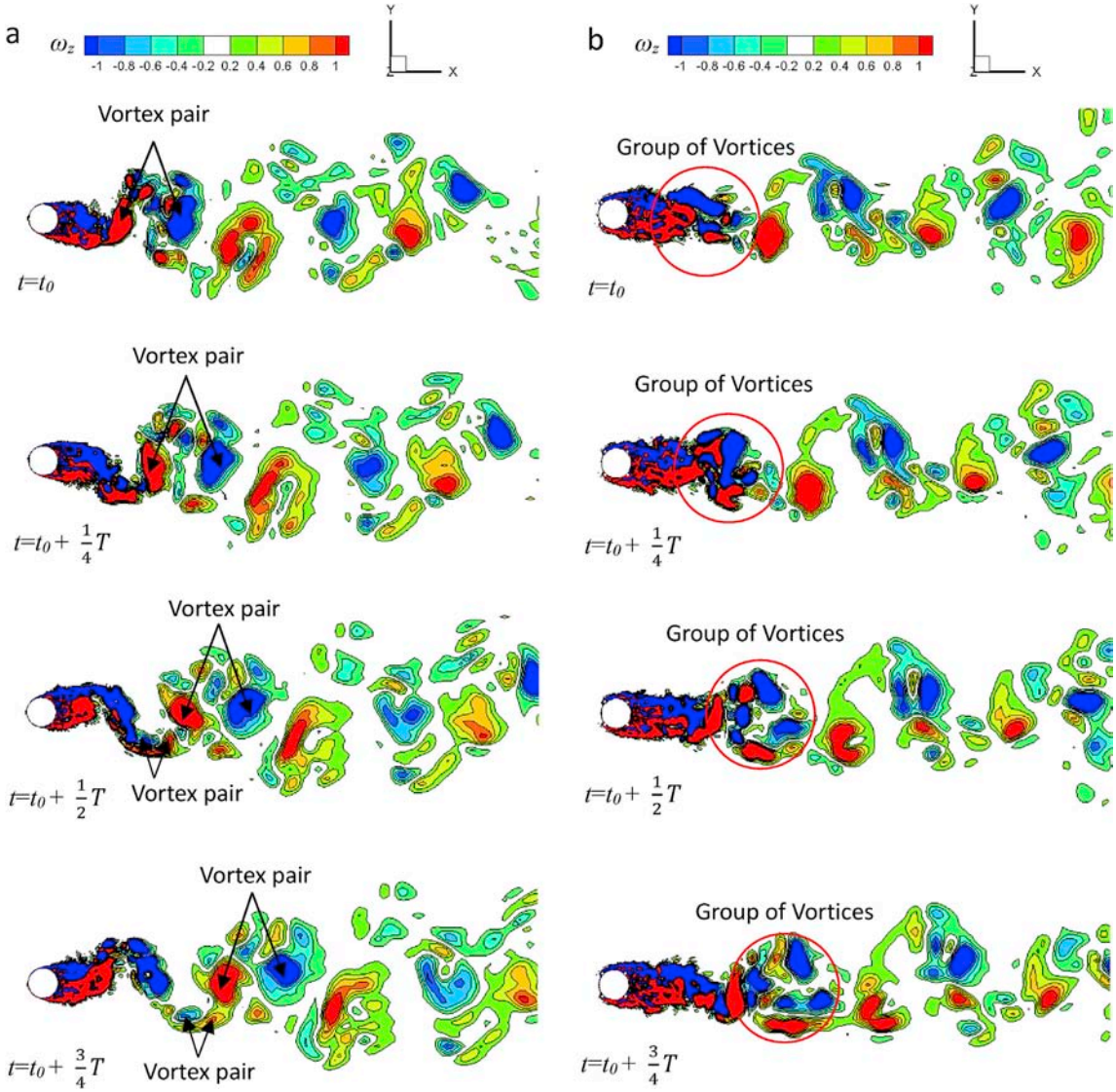

Fig. 13. Wake patterns around cylinders for different phases: (a) for the bare cylinder at $U_r = 5.7$; (b) for the wired cylinder at $U_r = 6.2$.

Table 3
Non-dimensional aerodynamic coefficients for the bare and wired cylinders.

	$C_{D\ mean}$	$C_{L\ rms}$	St
Bare cylinder ($d/D = 0$)	1.2504	0.5128	0.1946
Wired cylinder ($d/D = 0.1$)	1.2715	0.0677	0.1610
Ratio	1.02	0.13	0.83

that the phenomenon of phase jump for the wired cylinder happens at a higher reduced velocity than that for the bare cylinder. It implies that there is still a synchronization state for the wired cylinder, although the vibration amplitude has been reduced by the helical wires.

The flow patterns in the wake of bare and wired cylinders for different phases in a cycle of oscillation are visualized by the non-dimensional spanwise vorticity of middle plane $z/D = 2$ defined as $\omega_z = (\partial u_2/\partial x_1 - \partial u_1/\partial x_2)/(U/D)$ as shown in Fig. 13. The vortices formed in the wake of an oscillating cylinder are associated with the amplitude ratio A/D and the reduced frequency fD/U, as suggested by Williamson and Roshko (1988). The terminologies of certain wake patterns induced by body motion were introduced in Williamson and Roshko (1988), including the 2S mode (comprising 2 single vortices formed per cycle of body motion, like the classic Karman street) and the 2P mode (comprising 2 vortex pairs formed per cycle of body motion). The 2S mode is always found in the initial branch and changes into the 2P mode at the synchronization state (Blackburn et al., 2000; Lucor et al., 2005; Pan et al., 2007), which is reproduced by the present simulation as shown in Fig. 13 (a). For the wired cylinder, it is found that the vortex is destroyed by the wires so that the vortex is shed as a group of vortices instead of 2S or 2P modes at the near wake region as shown in Fig. 13(b). However, the group of vortices gradually merges into a single vortex in the farther wake region, so that there is still a VIV-like vibration although the amplitude is quite small. Such destruction of regular vortex shedding and extension of distance for the formation of Karman street were also found in the PIV experiment for the cylinder with helical strakes (Bearman and Brankovic, 2004; Korkischko and Meneghini, 2010; Zhou et al., 2011).

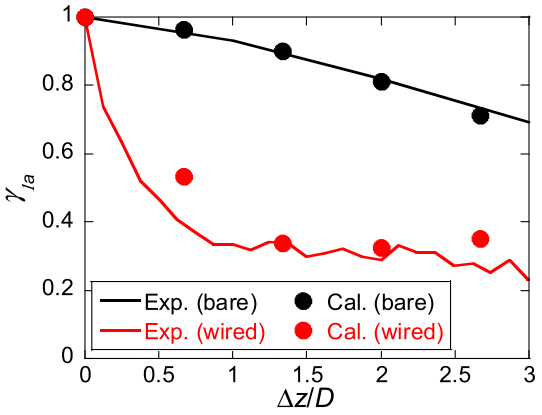

Fig. 14. Variation of the correlation coefficient of lift forces with the distance from the cross section 1 (CS1).

3.3. Effect of helical wires on the steady aerodynamic forces of circular cylinder

The aerodynamic forces, which are the main cause of vibration, are investigated to clarify the effect of helical wires on the suppression VIV. Weaver (1959) studied the VIV of circular cylinder with the helical wires by wind tunnel test and found that the lift force was reduced by the helical wires. The predicted aerodynamic force coefficients $C_{D\ mean}$, $C_{L\ rms}$ and Strouhal number St for cylinders with and without helical wires with $Re = 16000$ are listed in Table 3. It is noticed that for the cylinder with wires of $d/D = 0.1$, $C_{D\ mean}$ increases only 2% compared with that of the bare cylinder, which avoids the shortage of helical stakes for the drag increasing effect (Korkischko et al., 2007), while the $C_{L\ rms}$ decreases 87% compared with that of the bare cylinder, which shows the strong suppression effect. The reduction ratio of $C_{L\ rms}$ is close to 0.11 for a wired cylinder with $d/D = 0.12$ by Weaver (1959). The reduction effect of $C_{L\ rms}$ was also found for the helical strakes by Branković and Bearman (2006). St decreases 17% since the equivalent diameter of the wired cylinder increases 20%.

The spanwise correlation coefficient of lift force also helps to explain the effect of helical wires on the suppression of VIV. Fig. 14 shows the variation of the correlation coefficient with the distance from the cross section 1 (CS1) for the bare and wired cylinders. The spanwise distribution of correlation coefficients for the bare cylinder shows agreement with the experimental data by Blackburn (1994). Since there is no result for the correlation coefficients of lift force for the wired or straked cylinders in the previous research, the correlation coefficients of wake velocity for a straked cylinder with $d/D = 0.12$ by Zhou et al. (2011) is used to compare with the present numerical results for the wired cylinder with $d/D = 0.1$. It is found that the correlation coefficients of wired cylinder decrease more rapidly than those of bare cylinder in the spanwise direction, which leads the reduction effect on the lift force and suppresses the vortex-induced vibration.

To understand the effect of helical wires, a bird view of the flow patterns in the wake of bare and wired cylinders are visualized by the iso-surfaces of the second negative eigenvalue e_2 of the tensor $\Gamma^2+\Omega^2$ as shown in Fig. 15, where $e_2 = \lambda_2/(U/D)^2$ with λ_2 being the dimensional eigenvalue and set as 0.2 to show the iso-surface. Γ and Ω are the symmetric and anti-symmetric parts of the velocity-gradient tensor. The location of the vortex core can be identified by this particular eigenvalue

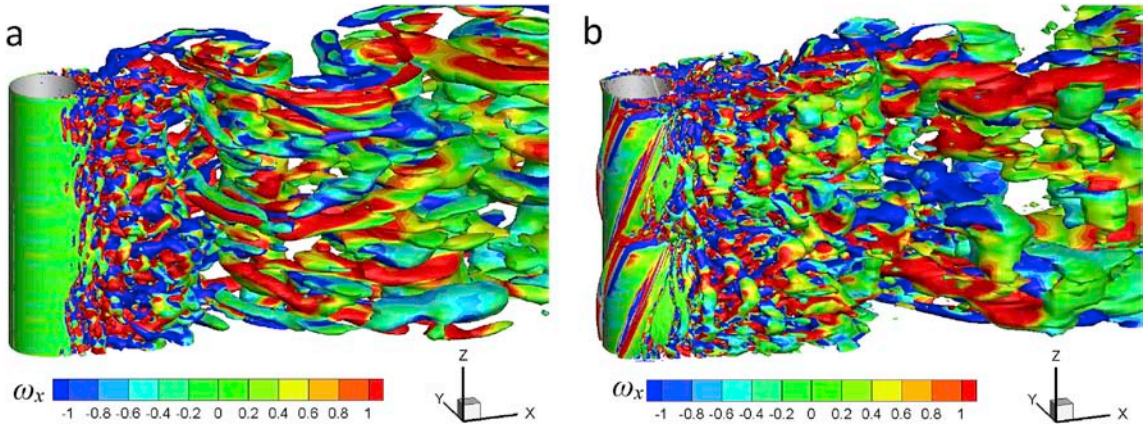

Fig. 15. Bird view of flow patterns around the cylinders: (a) bare cylinder; (b) wired cylinder.

(Zhao et al., 2014). These iso-surfaces are colored by the non-dimensional streamwise vorticity defined as $\omega_x=(\partial u_3/\partial x_2-\partial u_2/\partial x_3)/(U/D)$. It is noticed that the separation line is almost straight for the bare cylinder, but skewed by the helical wires. The contours of instantaneous non-dimensional spanwise vorticity ω_z at different cross sections of cylinders are shown in Fig. 16 to provide a more detailed illustration on the effect of helical wires. The transient time is chosen when the lift force gets its maximum value in one period. The Karman vortex streets behind the bare cylinder are well simulated and the flow patterns are similar at different cross sections as shown in Fig. 16(a). From the contour of instantaneous vorticity in Fig. 16(b), the vorticity of near wake is strengthened by the helical wires. The separation points at different cross sections are controlled by the helical wires, and the widths of wake are also influenced by the wires. As a result, the three-dimensionality of wake is obviously increased and thus the spanwise correlation of wake is decreased, which is one reason for VIV suppression by the wires helical.

3.4. Effect of helical wires on the unsteady aerodynamic forces of circular cylinder

The vibration-induced aerodynamic force is investigated to clarify the effect of aerodynamic damping on the VIV suppression. The aerodynamic force on the vibrating cylinder can be decomposed into two components

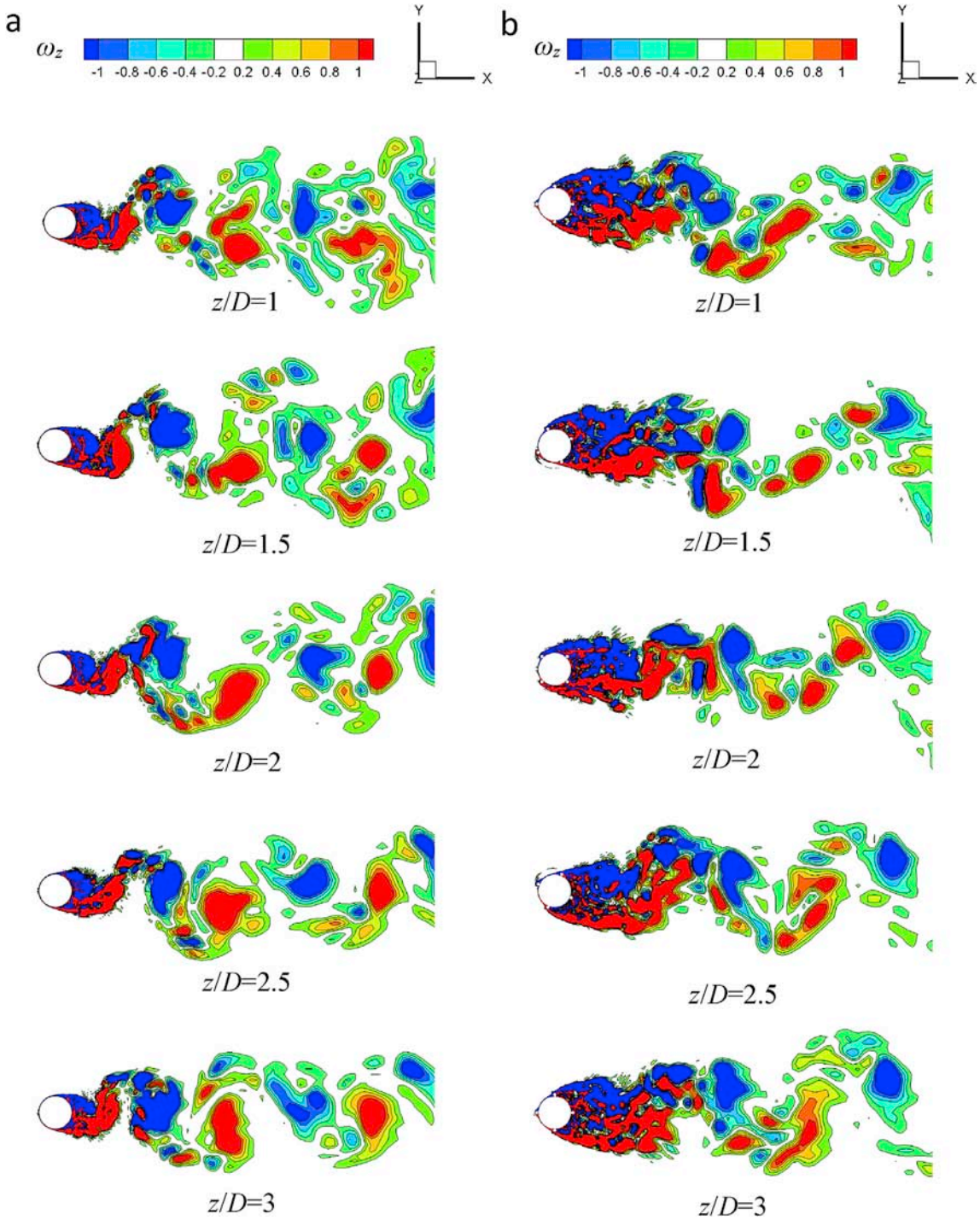

Fig. 16. Contours of instantaneous vorticity for different cross sections: (a) bare cylinder; (b) wired cylinder.

as (Li et al., 2018)

$$m\ddot{y} + c\dot{y} + ky = F_y(t) = F_b(t) + F_u(t, y, \dot{y}, \ddot{y}) \tag{13}$$

where the terms on the right-hand-side are the buffeting force F_b and the unsteady aerodynamic force or self-excited force F_u, which is a function of time t, displacement y, velocity $\dot{y}$ and acceleration $\ddot{y}$. The self-excited force F_u can be separated into two terms based on the orthogonality of displacement (or acceleration) and velocity. The force F_m related with the displacement y and the acceleration $\ddot{y}$ is called as the in-phase aerodynamic force. The force F_c related with the velocity $\dot{y}$ is called as the out-of-phase aerodynamic force and they are expressed as

$$F_u(t, y, \dot{y}, \ddot{y}) = F_m(t, y, \ddot{y}) + F_c(t, \dot{y}) \tag{14}$$

The in-phase and out-of-phase aerodynamic forces may be assumed as the linear functions of displacement and its derivative. The two terms on the right-hand-side of Eq. (14) then are expressed as

$$F_m(t, y, \ddot{y}) = -m_a\ddot{y} \tag{15}$$

$$F_c(t, \dot{y}) = -c_a\dot{y} \tag{16}$$

where m_a and c_a are called as the aerodynamic mass and the aerodynamic damping respectively since they lead to a change in the equivalent mass and the equivalent damping of system. Eq. (13) is rewritten as

$$(m + m_a)\ddot{y} + (c + c_a)\dot{y} + ky = F_b(t) \tag{17}$$

The unsteady aerodynamic forces can be derived based on the orthogonality of displacement and velocity as

$$m_a = -\frac{\int_0^T F_y(t)\ddot{y}(t)dt}{\int_0^T \ddot{y}(t)^2 dt} \tag{18}$$

$$c_a = -\frac{\int_0^T F_y(t)\dot{y}(t)dt}{\int_0^T \dot{y}(t)^2 dt} \tag{19}$$

The forced oscillation is a general method to identify the aerodynamic damping. Here, the cylinder is forced to oscillate sinusoidally as

$$y = A\sin(2\pi f_n t) \tag{20}$$

where A is the oscillating amplitude set as $0.1D$, which is a little lower than the free-vibration amplitude at the resonance velocity of bare cylinder. The oscillating frequency equals to the natural frequency of cylinder f_n. The total damping of system is defined as

$$c_{total} = c + c_a \tag{21}$$

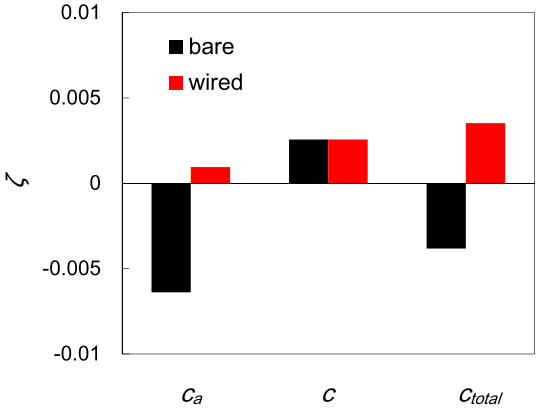

Fig. 17. Aerodynamic, structural and total damping ratios.

Fig. 17 shows the aerodynamic, structural and total damping ratios of system for the cylinder with and without the helical wires at the resonance velocity of bare cylinder $U_r = 5.7$. It is found that the aerodynamic damping for the bare cylinder is negative and leads a negative total damping of system. However, the aerodynamic damping for the wired cylinder is positive and causes a positive total damping of system. The negative total damping induces self-excited VIV for the bare cylinder, while the positive one suppresses this vibration for the helical wired cylinder. This is another reason for VIV suppression by the helical wires.

4. Conclusions

The mechanism of VIV suppression for circular cylinder by helical wires is investigated using LES turbulence model with dynamic mesh. A numerical model for the free-vibrating circular cylinders with and without helical wires is proposed and the amplitude of vibration is validated by the experimental data. The steady and unsteady aerodynamic forces on the cylinders with and without helical wires as well as the flow patterns are examined to clarify the mechanism of VIV suppression. The main conclusions are summarized as follows:

(1) The VIV amplitude of cylinder is effectively suppressed and the "lock in" is avoided by the helical wires of $d/D = 0.1$. The magnitude of lift force for the wired cylinder is reduced in the whole range of velocity, while the magnitude of drag force is kept at the same level. The phase jump happens at the resonant regime for the bare cylinder and moves to a higher reduced velocity for the wired cylinder due to the decrease of vortex shedding frequency.

(2) The fluctuating lift forces and their spanwise correlation for the stationary cylinder with the helical wires are significantly reduced because the wires skew the vortex separation line on the cylinder, which is one reason for VIV suppression by the helical wires. The drag force coefficients for both stationary cylinders with and without the helical wires are almost constant. The vortex shedding frequency of the wired cylinder is also decreased by the helical wires since the equivalent diameter of the wired cylinder is increased.

(3) The aerodynamic damping for the vibrated cylinder without the helical wires is negative with a vibration amplitude $A/D = 0.1$ at the resonance velocity, which reduces the total damping ratio of system to a negative value. However, the aerodynamic damping for the vibrated cylinder with the helical wires is positive, which is another reason for VIV suppression by the helical wires.

Author contributions section

Takeshi ISHIHARA: Conceptualization; Formal analysis; Funding acquisition; Methodology; Project administration; Resources; Supervision; Writing – review & editing. **Tian LI:** Data curation; Formal analysis; Investigation; Software; Validation; Visualization; Writing – original draft.

Declaration of competing interest

The authors declare that they have no known competing financial interests or personal relationships that could have appeared to influence the work reported in this paper.

References

Allen, D.W., Henning, D.L., Lee, L., 2006. High Reynolds number flow tests of flexible cylinders with helical strakes. In: 25th International Conference on Offshore Mechanics and Arctic Engineering. American Society of Mechanical Engineers, pp. 359–367.

ANSYS Inc, 2015. ANSYS FLUENT 16.2 Theory Guide.

Arif, M.R., Hasan, N., 2019. Vortex shedding suppression in mixed convective flow past a square cylinder subjected to large-scale heating using a non-Boussinesq model. Phys. Fluids 31 (2), 023602.
Assi, G.R.S., Bearman, P.W., Meneghini, J.R., 2010. On the wake-induced vibration of tandem circular cylinders: the vortex interaction excitation mechanism. J. Fluid Mech. 661, 365–401.
Bahmani, M.H., Akbari, M.H., 2010. Effects of mass and damping ratios on VIV of a circular cylinder. Ocean. Eng. 37 (5–6), 511–519.
Bearman, P.W., 2011. Circular cylinder wakes and vortex-induced vibrations. J. Fluids Struct. 27 (5–6), 648–658.
Bearman, P., Branković, M., 2004. Experimental studies of passive control of vortex-induced vibration. Eur. J. Mech. B Fluid 23 (1), 9–15.
Blackburn, H.M., 1994. Effect of blockage on spanwise correlation in a circular cylinder wake. Exp. Fluid 18 (1–2), 134–136.
Blackburn, H.M., Govardhan, R.N., Williamson, C.H.K., 2000. A complementary numerical and physical investigation of vortex-induced vibration. J. Fluids Struct. 15 (3–4), 481–488.
Branković, M., Bearman, P.W., 2006. Measurements of transverse forces on circular cylinders undergoing vortex-induced vibration. J. Fluids Struct. 22 (6–7), 829–836.
Carmo, B.S., Gioria, R.S., Korkischko, I., Freire, C.M., Meneghini, J.R., 2012. Two-and three-dimensional simulations of the flow around a cylinder fitted with strake. In: Proceedings of the ASEM 31st International Conference on Ocean, Offshore and Arctic Engineering, Rio de Janeiro, Brazil, pp. 781–790.
Constantinides, Y., Oakley, O.H., 2006. Numerical prediction of bare and straked cylinder VIV. In: Proceedings of the OMAE 2006 25th International Conference on Offshore Mechanics and Arctic Engineering, Hamburg, Germany.
Feng, C.C., 1968. The Measurement of Vortex Induced Effects in Flow Past Stationary and Oscillating Circular and D-Section Cylinders, Master Dissertation. University of British Columbia.
Ferziger, J.H., Peric, M., 2002. Computational Methods for Fluid Dynamics. Springer Science & Business Media.
Govardhan, R.N., Williamson, C.H.K., 2006. Defining the 'modified Griffin plot'in vortex-induced vibration: revealing the effect of Reynolds number using controlled damping. J. Fluid Mech. 561, 147–180.
Griffin, O.M., 1980. Vortex-excited cross-flow vibrations of a single cylindrical tube. J. Press. Vessel Technol. 102 (2), 158–166.
Gsell, S., Bourguet, R., Braza, M., 2016. Two-degree-of-freedom vortex-induced vibrations of a circular cylinder at Re= 3900. J. Fluids Struct. 67, 156–172.
Guilmineau, E., Queutey, P., 2002. A numerical simulation of vortex shedding from an oscillating circular cylinder. J. Fluids Struct. 16 (6), 773–794.
Hover, F.S., Tvedt, H., Triantafyllou, M.S., 2001. Vortex-induced vibrations of a cylinder with tripping wires. J. Fluid Mech. 448, 175–195.
Kakade, A.A., Singh, S.K., Panigrahi, P.K., Muralidhar, K., 2010. Schlieren investigation of the square cylinder wake: joint influence of buoyancy and orientation. Phys. Fluids 22 (5), 054107.
Kang, Z., Ni, W., Sun, L., 2017. A numerical investigation on capturing the maximum transverse amplitude in vortex induced vibration for low mass ratio. Mar. Struct. 52, 94–107.
Khalak, A., Williamson, C.H., 1997. Investigation of relative effects of mass and damping in vortex-induced vibration of a circular cylinder. J. Wind Eng. Ind. Aerodyn. 69, 341–350.
Khalak, A., Williamson, C.H., 1999. Motions, forces and mode transitions in vortex-induced vibrations at low mass-damping. J. Fluids Struct. 13 (7–8), 813–851.
Korkischko, I., Meneghini, J.R., Gioria, R.S., Jabardo, P.J., Casaprima, E., Franciss, R., 2007. An experimental investigation of the flow around straked cylinders. In: Proceedings of the 26th International Conference on Offshore Mechanics and Arctic Engineering. American Society of Mechanical Engineers Digital Collection, San Diego, California, USA, pp. 641–647.
Korkischko, I., Meneghini, J.R., 2010. Experimental investigation of flow-induced vibration on isolated and tandem circular cylinders fitted with strakes. J. Fluids Struct. 26 (4), 611–625.
Kubo, Y., Yuki, Y., Ishii, H., Hatakenaka, S., Kawato, C., 2012. A feature on wake galloping of a bridge in full sized parallel cable model. J. Struct. Eng. 58A, 518–527 (in Japanese).
Leontini, J.S., Thompson, M.C., Hourigan, K., 2006. The beginning of branching behaviour of vortex-induced vibration during two-dimensional flow. J. Fluids Struct. 22 (6–7), 857–864.
Li, T., Yang, Q., Ishihara, T., 2018. Unsteady aerodynamic characteristics of long-span roofs under forced excitation. J. Wind Eng. Ind. Aerodyn. 181, 46–60.
Lim, H.C., Lee, S.J., 2002. Flow control of circular cylinders with longitudinal grooved surfaces. AIAA J. 40 (10), 2027–2036.
Lucor, D., Foo, J., Karniadakis, G.E., 2005. Vortex mode selection of a rigid cylinder subject to VIV at low mass-damping. J. Fluids Struct. 20 (4), 483–503.
Navrose, Mittal, S., 2013. Free vibrations of a cylinder: 3-D computations at Re= 1000. J. Fluids Struct. 41, 109–118.
Nicoud, F., Ducros, F., 1999. Subgrid-scale stress modelling based on the square of the velocity gradient tensor. Flow, Turbul. Combust. 62 (3), 183–200.
Norberg, C., 2003. Fluctuating lift on a circular cylinder: review and new measurements. J. Fluids Struct. 17 (1), 57–96.
Pan, Z.Y., Cui, W.C., Miao, Q.M., 2007. Numerical simulation of vortex-induced vibration of a circular cylinder at low mass-damping using RANS code. J. Fluids Struct. 23 (1), 23–37.
Pinto, A., Broglia, R., Di Mascio, A., Campana, E.F., Rocco, P., 2006. Numerical investigation of the unsteady flow at high Reynolds number over a marine riser with helical strakes. In: 25th International Conference on Offshore Mechanics and Arctic Engineering. American Society of Mechanical Engineers, pp. 587–595.
Pontaza, J.P., Menon, R.G., Chen, H.C., 2009. Three-dimensional numerical simulations of flows past smooth and rough/bare and helically straked circular cylinders allowed to undergo two degree-of-freedom motions. J. Offshore Mech. Arct. Eng. 131 (2), 021301.
Prsic, M.A., Ong, M.C., Pettersen, B., Myrhaug, D., 2014. Large Eddy Simulations of flow around a smooth circular cylinder in a uniform current in the subcritical flow regime. Ocean. Eng. 77, 61–73.
Quen, L.K., Abu, A., Kato, N., Muhamad, P., Sahekhaini, A., Abdullah, H., 2014. Investigation on the effectiveness of helical strakes in suppressing VIV of flexible riser. Appl. Ocean Res. 44, 82–91.
Raghavan, K., Bernitsas, M.M., 2011. Experimental investigation of Reynolds number effect on vortex induced vibration of rigid circular cylinder on elastic supports. Ocean. Eng. 38 (5–6), 719–731.
Sarpkaya, T., 2004. A critical review of the intrinsic nature of vortex-induced vibrations. J. Fluids Struct. 19 (4), 389–447.
Sarwar, M.W., Ishihara, T., 2010. Numerical study on suppression of vortex-induced vibrations of box girder bridge section by aerodynamic countermeasures. J. Wind Eng. Ind. Aerodyn. 98 (12), 701–711.
Scruton, C., Walshe, D. E. J., 1963. Stabilisation of wind-excited structures. U.S. Patent No. 3,076,533. Washington, DC: U.S. Patent and Trademark Office.
Singh, S.P., Mittal, S., 2005. Vortex-induced oscillations at low Reynolds numbers: hysteresis and vortex-shedding modes. J. Fluids Struct. 20 (8), 1085–1104.
Singh, S.P., Biswas, G., 2013. Vortex induced vibrations of a square cylinder at subcritical Reynolds numbers. J. Fluids Struct. 41, 146–155.
Smagorinsky, J., 1963. General circulation experiments with the primitive equations: I. The basic experiment. Mon. Weather Rev. 91 (3), 99–164.
Tu, J., Zhou, D., Bao, Y., Fang, C., Zhang, K., Li, C., Han, Z., 2014. Flow-induced vibration on a circular cylinder in planar shear flow. Comput. Fluids 105, 138–154.
Wanderley, J.B., Soares, L.F.N., 2015. Vortex-induced vibration on a two-dimensional circular cylinder with low Reynolds number and low mass-damping parameter. Ocean. Eng. 97, 156–164.
Wang, E., Xiao, Q., Incecik, A., 2017. Three-dimensional numerical simulation of two-degree-of-freedom VIV of a circular cylinder with varying natural frequency ratios at Re= 500. J. Fluids Struct. 73, 162–182.
Weaver, J., 1959. Experimental Investigation of Wind-Induced Vibrations in Antenna Members (No. GR-75-4). Massachusetts Institute of Technology: Lincoln Laboratory.
West, G.S., Apelt, C.J., 1982. The effects of tunnel blockage and aspect ratio on the mean flow past a circular cylinder with Reynolds numbers between 10^4 and 10^5. J. Fluid Mech. 114, 361–377.
West, G.S., Apelt, C.J., 1993. Measurements of fluctuating pressures and forces on a circular cylinder in the Reynolds number range 10^4 to 2.5×10^5. J. Fluids Struct. 7 (3), 227–244.
Williamson, C.H.K., 1988. The existence of two stages in the transition to three-dimensionality of a cylinder wake. Phys. Fluids 31 (11), 3165–3168.
Williamson, C.H.K., Govardhan, R., 2008. A brief review of recent results in vortex-induced vibrations. J. Wind Eng. Ind. Aerodyn. 96 (6–7), 713–735.
Williamson, C.H.K., Roshko, A., 1988. Vortex formation in the wake of an oscillating cylinder. J. Fluids Struct. 2 (4), 355–381.
Zafar, F., Alam, M.M., 2019. Flow structure around and heat transfer from cylinders modified from square to circular. Phys. Fluids 31 (8), 083604.
Zdravkovich, M.M., 1981. Review and classification of various aerodynamic and hydrodynamic means for suppressing vortex shedding. J. Wind Eng. Ind. Aerodyn. 7 (2), 145–189.
Zhao, M., Cheng, L., Zhou, T., 2013. Numerical simulation of vortex-induced vibration of a square cylinder at a low Reynolds number. Phys. Fluids 25 (2), 023603.
Zhao, M., Cheng, L., An, H., Lu, L., 2014. Three-dimensional numerical simulation of vortex-induced vibration of an elastically mounted rigid circular cylinder in steady current. J. Fluids Struct. 50, 292–311.
Zhou, T., Razali, S.M., Hao, Z., Cheng, L., 2011. On the study of vortex-induced vibration of a cylinder with helical strakes. J. Fluids Struct. 27 (7), 903–917.